

Framework of Maximum Solar Energy Conversion Using Lyapunov-Based Model Reference Adaptive Control Technique in Stochastic Weather Conditions

Deepak Kumar Singh,* Ashok Kumar Akella, and Saibal Manna

The solar photovoltaic (PV) energy generation technology has grown rapidly. Herein, a novel continuous-time Lyapunov-based model reference adaptive control (LB-MRAC) technique is suggested for determining the duty cycle of boost converter to maintain maximum power point (MPP) of the solar PV panel. For ensuring the fast-tracking speed, the reference voltage of, respectively, MPP is calculated using perturb and observe (PO) and input to the MRAC technique. Using MATLAB/Simulink, the performances of the LB-MRAC maximum power point tracking are comparatively analyzed with PO, incremental conductance, and adaptive neuro-fuzzy inference system under diverse testing modes such as stand-alone, partial shading, grid integrated, and real time. The proposed technique tracks MPP in just 3.7 ms having tracking efficacy between 99.15% and 99.59% under highly fluctuating irradiance and temperature with load uncertainties. In partial shading mode, four patterns (3×1 PV string) are devised and determined where that the suggested approach monitors the global MPP in merely 0.04 s with the highest power tracked and the least amount of shading loss. Next, the efficacy is checked in a three-phase 50 kW grid-integrated mode under realistic weather. Finally, the performance of the suggested continuous-time LB-MRAC technique is experimentally corroborated employing OPAL-RT(OP4510) in the real-time mode.

1. Introduction

1.1. Motivation and Background

A future for clean energy is being offered by the rising demand for renewable energy, solar, and wind energy are the driving forces behind this sustainable energy revolution. It is acknowledged that the power produced by the sun is secure and freely accessible on the earth surface. Currently, solar power meets

1.7% of the world's electricity demand, and by 2025, the number is expected to rise to 1 TW.^[1] Globally, the use of solar photovoltaic (PV) electricity has grown significantly in recent years as per data released in the Renewable Capacity Statistics 2023 by the International Renewable Energy Agency, as shown in Figure 1.^[2]


The efficiency of PV energy conversion is significantly influenced by temperature and solar irradiation. When all PV modules acquire the same solar irradiance and temperature, the P–V characteristic has one peak, and it is called the uniformly shaded PV panel. Since trees, clouds, raindrops, and structures that block the sun from reaching the PV panel cause it to be partially shaded. Multiple peaks can be observed on the P–V characteristic, including local MPP (LMPP) and global MPP (GMPP).^[3] Figure 2 shows the P–V curve of the uniformly and partially shaded PV panel. Consequently, maximum power point tracking (MPPT) control is essential for a PV system, and there have been many suggested MPPT algorithms, including

conventional and advanced techniques. In 1968, first time MPPT was used in the spacecraft for converting solar power into usable form. Numerous complex algorithms were developed in the years since that perform better from the standpoint of efficiency, tracking speed, and accuracy, as documented in the literature.^[4]

In the recent years, many optimization-based MPPT methods typically seek out true maximum power point (MPP) in dynamic environments. Conventional MPPT methods like incremental conductance (INC) and perturb and observe (PO) have been extensively studied. These algorithms are simple, cheap, and track the MPP correctly in uniform atmospheric conditions. Their major drawbacks are oscillations near the MPP and inefficient in partial shading conditions (PSC) by confining to the nearest LMPP.^[5] In perspective of these drawbacks, many advanced MPPT algorithms were implemented such as artificial intelligence (e.g., fuzzy logic controller (FLC), artificial neural networks, adaptive neuro-fuzzy inference system (ANFIS)) and metaheuristic techniques (e.g., genetic algorithm (GA), particle swarm optimization (PSO)).^[6,7] These methods significantly improve the performance of the solar PV under stochastic weather circumstances. However, such approaches are complex,

D. K. Singh, A. K. Akella
Department of Electrical Engineering
National Institute of Technology Jamshedpur
Jamshedpur, Jharkhand 831014, India
E-mail: 2020rsee003@nitjsr.ac.in

S. Manna
Department of Electrical and Electronics Engineering
ABES Engineering College
Ghaziabad, Uttar Pradesh 201009, India

 The ORCID identification number(s) for the author(s) of this article can be found under <https://doi.org/10.1002/ente.202300775>.

DOI: 10.1002/ente.202300775

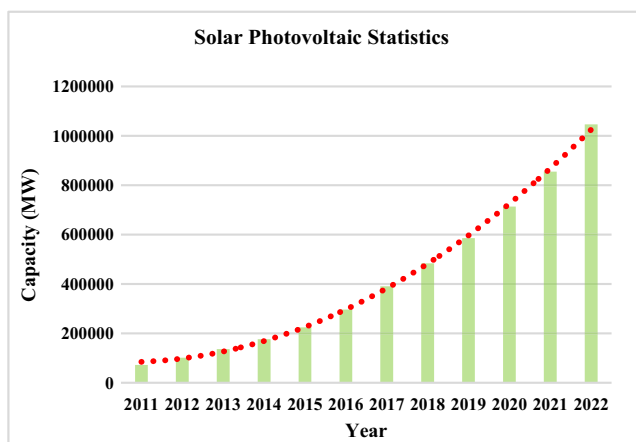


Figure 1. Worldwide capacity of installed solar PV.

expensive, require prior knowledge, time consuming in computing, and complexity in hardware implementation.^[8] Thus, the primary objective of the study is to devise and execute a hybrid and efficient control scheme that can manage abnormal climatic circumstances and do away with the drawbacks of both conventional and advanced techniques.

1.2. Status Quo of MPPT Techniques

Several research endeavors have been dedicated to enhancing the response of PV system through development of various MPPT techniques. In order to monitor the MPP, a resilient sliding mode control (SMC) deployed, which incorporates the quantized input hysteresis and resolves the chattering problem, i.e., commonly encountered in conventional SMC. The method exhibits superior performance in simulations as compared to conventional controllers, thereby showcasing its adeptness in mitigating the impact of chattering and extraneous disturbances. The observed enhancements in convergence time of 1.8 s and tracking efficiency of 99.1% under fluctuating radiation conditions represent noteworthy advancements over the corresponding metrics of ANFIS, variable step-INC, SMC, and memetic slap swarm optimization.^[9] A discrete proportional integral derivative (PID) optimized using the gray wolf optimization presented, and its efficacy is assessed with PO, INC, wolf optimization algorithm, simulated annealing, and PSO. The suggested MPPT exhibits superior performance as compared to other methods, with an average power output improvement of 6% under diverse temperature, radiation, and load conditions. The methodology yielded

minimum average settling duration of 0.175 s through different levels of irradiance. The drawbacks associated with the methodology include significant computational overhead, increased expenses, and necessitated exploration of the search domain.^[10]

A pioneering technique, which leverages the Nelder–Mead algorithm introduced. It exhibits superior performance as compared to the bat optimization algorithm, artificial bee colony (ABC), and deterministic PSO regarding success rate and accuracy for all analyzed shading scenarios, as demonstrated using simulation and experimental outcomes. The mean power dissipation and precision of tracking are 18.26 W and 99.89%, correspondingly. Moreover, its rate of tracking is approximately three times higher than alternative techniques. Though, the validation of the methodology is pending for three-phase grid-integrated scenarios.^[11] An approach based on improved squirrel search algorithm presented, exhibiting a 50% improvement in tracking time over the conventional SSA. Furthermore, the suggested technique was evaluated against the widely recognized GA and PSO, using three different shading conditions (wherein 3 PV modules are linked in a series). The experimental verification and effectiveness of the suggested technique showcases its adeptness in following the GMPP tracking of 0.66 s and an efficacy of 99.48%.^[12]

A method for achieving maximal power amid varying load, irradiance, and temperature scenario involves utilizing a two-stage MPPT approach. At first, a single input single output FLC with INC is used to produce a continuous reference voltage. An optimal integrator controller (OIC) is utilized for regulating feedback voltage control of the PV plant. The utilization of Routh's criterion is imperative for the purpose of tuning the OIC while taking into account of the fluctuations in load. The simulation findings corroborate the efficacy of the approach in comparison to other widely used methods, including INC-OIC, PO, and INC with direct control and adaptive PO and INC with direct control. The demonstrated supremacy of the controller is attributed to its exceptional efficacy, surpassing 98% in all conditions.^[13] An MPPT controller utilizing the modified butterfly optimization (MBO) algorithm suggested and it necessitates only one tuning parameter, which is reliant on open circuit voltage. The experimental outcomes indicate that various shading configurations can be detected within an average time of less than 1 s, with a 99.85% efficacy rate, while avoiding the reuse of identical locations in the search area. Upon application to the uniformly shaded pattern, the suggested technique resulted in a 47.20% enhancement in tracking speed. The load fluctuation response is improved by 86.15% while maintaining the butterfly positions.^[14]

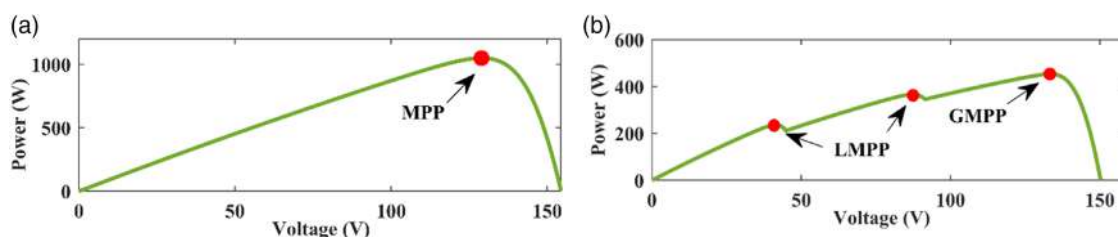


Figure 2. Solar photovoltaic panel P–V characteristics a) uniformly and b) partially shaded.

A technique utilizing dragonfly optimization algorithm (DOA) suggested for solar PV that are connected to the grid, and it also operates efficiently even in PSC. The efficacy of the suggested technique was evaluated against established methodologies, including fruit fly optimization-general regression neural network, adaptive cuckoo search algorithm, PSO, adaptive PSO, and PO, under two distinct shading configurations involving a series connection of three PV modules. The simulation findings indicate that DOA method exhibits superior convergence time in comparison to alternative methodologies, with recorded durations of 0.29 and 0.32 s for two distinct patterns.^[15] A coarse and fine control approach for PO algorithm suggested to ensure ease of implementation. In addition to its simplicity, the algorithm effectively mitigates all the drawbacks associated with the conventional PO technique, including prolonged tracking time, reduced efficiency, heightened oscillation, and power dissipation. The algorithm comprises of three unique control modes that facilitate rapid convergence through modes 1 and 2, while mode 3 controls fluctuations in steady state. The simulation findings indicate that the methodology offers reduced tracking speed, oscillations, power dissipation, and enhanced tracking capability in contrast to the drift-free and conventional PO methodologies. Despite that the technique efficacy under PSC and grid integration is not discussed.^[16] The investigation entails the comprehensive development of an adaptive robust fuzzy proportional-integral (ARFPI) controller, i.e., adaptive and robust, with a fuzzy proportional-integral component, to optimize MPPT performance of solar PV system. The assessment of ARFPI performance in the presence of fluctuating temperature and irradiation is based on the analysis of steady-state ripple and undershoot. Furthermore, a comparative analysis is conducted between the suggested algorithm and conventional techniques including INC, PID, and PO to evaluate its efficacy. The experimental findings indicate that the ARFPI regulator exhibits superior performance characteristics, including reduced undershoot and ripple. Therefore, it is a viable option for deployment as an MPPT controller in PV applications.^[17]

A PV system performance enhancement technique called adjustable variable step-based backstepping (VS-BS) suggested. The concept underlying the amalgamation of the dual MPPT techniques is to enhance the tracking speed and precision while maintaining the simplicity of the arrangement. The VS-BS strategy can precisely detect the MPP without any overshoot and minimal fluctuation under varying temperature, irradiance with load circumstances. Nevertheless, the effectiveness of the VS-BS method under PSC and grid-integration has not been addressed.^[18] To achieve MPP efficiently, authors suggested a FLC that utilizes an improved bat algorithm (IBA). In order to perform the fine-tuning of the FLC membership functions, IBA is employed. The simulation results of various case studies confirmed the supremacy of the recommended method as compared to PO, FLC, and INC. The results indicate that the suggested methodology can enhance the system's power output by 2–8% when compared to conventional techniques under different irradiance and temperature circumstances. Despite that, the performance of the IBA-FLC remains untested amidst swiftly fluctuating irradiance, temperature, and load conditions.^[19]

This paper introduces a reduced oscillation-based PO (ROPO) MPPT algorithm and compares performance parameters with traditional PO and INC methods. The ROPO technique has a tracking efficacy of 99.06–99.80%, PO ranges from 93.37% to 97.81%, and INC ranges from 66.23% to 98.55% across all states. The suggested MPPT technique has minimal oscillations near MPP and lower tracking power loss compared to PO and INC, which makes it most effective. The ROPO method reaches steady state in 0.018 s, and it is 5 times and 15 times faster than PO and INC techniques, respectively. The recommended approach has the lowest MPP error rates compared to PO and INC approaches. The suggested technique is validated using a three-phase grid, resulting in transmitting grid current power quality meeting IEEE 519 benchmark. The ROPO method is efficient and straightforward to implement, as expressed by time domain analysis. It also reduces computational strain on the system. The ROPO technique's main drawback is partial shading incompatibility.^[20]

A hybrid ANFIS-PSO MPPT is designed employing zeta converter to precisely track MPP with oscillation free for grid-integrated solar PV. The recommended MPPT performs well in contrast to PO, ABC, PSO, and Ant colony optimization under fluctuating atmospheric scenario. The tracking efficiency of the recommended ANFIS-PSO, ABC, and PSO is 98.35%, 97.11%, and 94.88%, respectively. Using MATLAB-interfaced dSPACE, the recommended ANFIS-PSO method was experimentally evaluated, and the outcomes confirmed the flawless implementation of the control mechanism.^[21]

1.3. Main Contributions

As per through literature review, it is recognized that none of the author corroborated MPPT performance taking into account stochastic weather scenarios such as simultaneously fluctuating radiation and temperature with load uncertainties; partial-shaded and grid-integrated with realistic weather. These facts motivated to design a novel continuous-time Lyapunov-based MRAC MPPT structure for solar PV system. The objective of this research is to design continuous-time Lyapunov-based model reference adaptive control (LB-MRAC) control scheme for second-order solar PV system, which is based on Lyapunov stability theorem to achieve fast tracking speed, high efficiency, less steady-state oscillation, ripple free, and negligible power loss.

For each MPP, a reference voltage is generated, and it is updated on the regular basis, in comparison with varying PV voltage led by stochastic weather conditions. The difference between PV voltage and updated reference, which is calculated using PO algorithm, is the input to the LB-MRAC technique. Fitting suitable controller parameters is the art of the proposed LB-MRAC technique. By choosing the proper adaptation laws, this is accomplished. During adaptation, the proposed controller parameters are adjusted based upon the error between the reference and plant models. The adaptive laws ought to be able to predict the controller's unknowable characteristics besides maintaining close loop stability. In order to achieve this goal, Lyapunov stability theory is employed. The continuous-time LB-MRAC module generates a reference signal to modulate duty cycle of the

pulse width modulation (PWM) waveform, which is subsequently applied to the boost converter. This control scheme guarantees that the solar PV system operating at its MPP at all times.

Using MATLAB/Simulink, the proposed MPPT control approach is modeled and designed for the solar PV system. The assessment framework is devised taking into account the real-world situations, simulation, and experimental studies are accomplished through various testing modes. The methodological framework of the proposed work is depicted in Figure 3.

2. Solar Energy Conversion System

2.1. Solar PV Model

The main components of a solar PV power system are PV panels, which are typically combined in series and/or shunt to increase power output and voltage generation. PV cell is conceptualized as a current source coupled with a diode, a series (R_s), and a shunt resistance (R_p), illustrated in Figure 4.

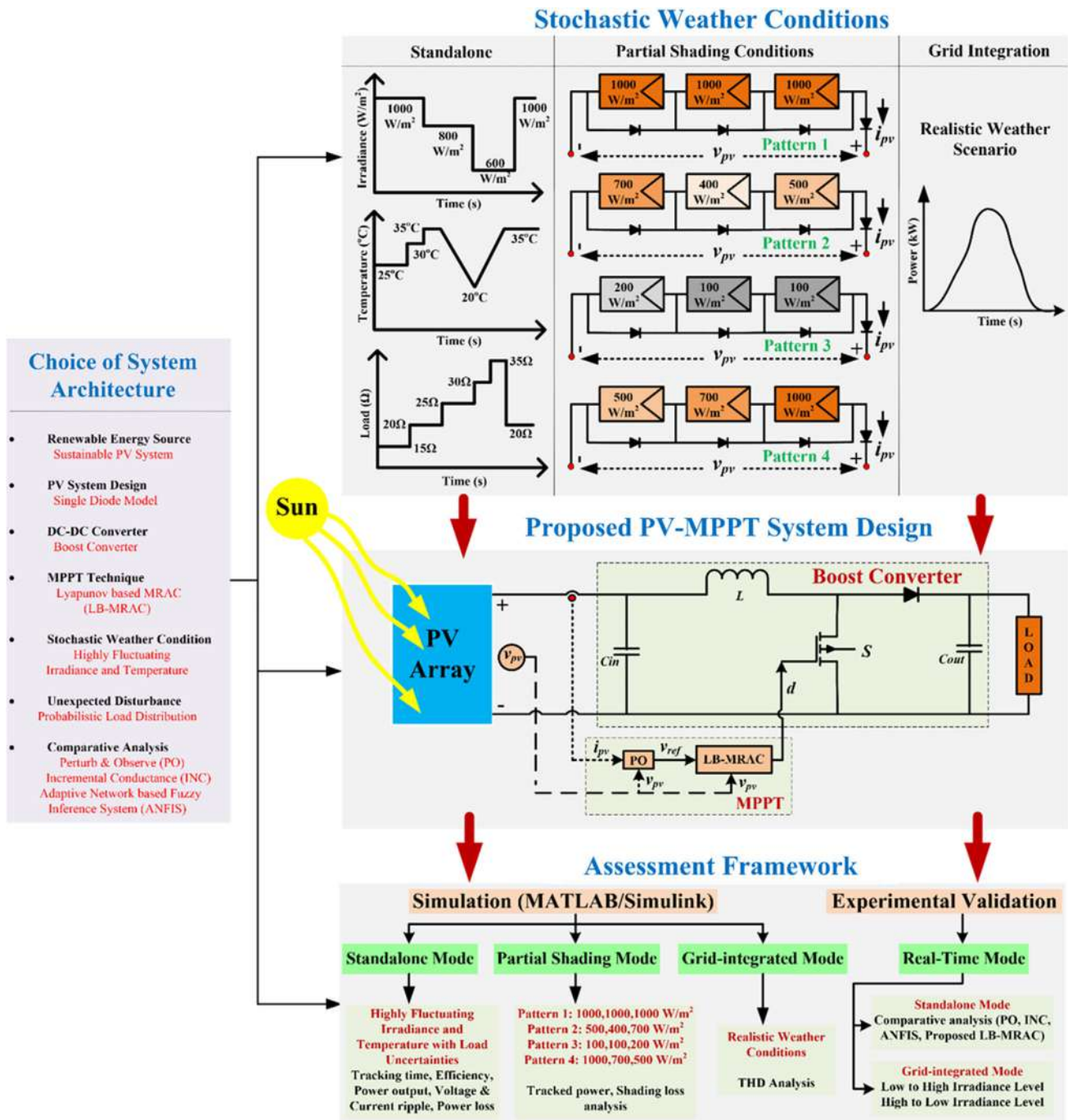


Figure 3. Methodological framework of the proposed research.

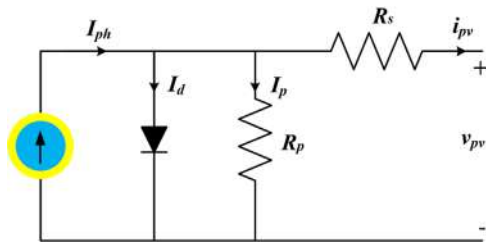


Figure 4. Circuit diagram of the PV model.

The mathematical relationship among PV array output current (i_{pv}), photo current (I_{ph}), diode current (I_d), and current through the parallel branch (I_p) are made using equivalent circuit.^[22] The photo current is also correlated with radiation and temperature given in Equation (1) and (2). Here, K_t is temperature coefficient at 1000 W m^{-2} and 25°C , and T and T_a are standard and absolute ambient temperature, respectively. Next, G and G_{st} are irradiance (W m^{-2}) and standard irradiance correspondingly.

$$I_{ph} = I_{ph}(G)[1 + K_t(T - T_a)] \quad (1)$$

$$I_{ph}(G) = I \left(\frac{G}{G_{st}} \right) \quad (2)$$

2.2. PV with MPPT Concept: Small-Signal Analysis

In order to optimize the performance of the solar PV system, it is imperative to maintain constant monitoring of the MPP at the P-V characteristics through the implementation of a suitable MPPT technique utilizing a boost converter. It is used for impedance matching to withdraw the optimum amount of power from the PV panel.^[23] Figure 5 depicts the PV system connected to boost converter with MPPT and load. The switching transistor S receives the duty cycle (d) from the MPPT, which senses the voltage and current of the solar PV panel. The array voltage influences the transistor's duty cycle through

$$v_{pv} = i_{pv} \times R_L(1 - d)^2 \quad (3)$$

where R_L is the resistive load. Both the i_{pv} and v_{pv} contain DC components (I_{pv} and V_{pv}) in addition to ripple components (\hat{i}_{pv} and \hat{v}_{pv}).

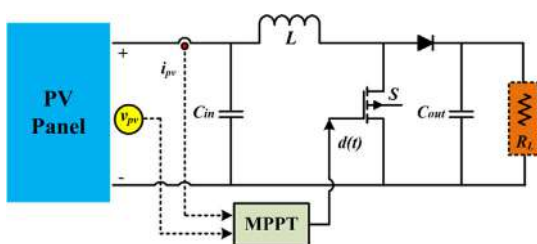


Figure 5. PV panel with MPPT and boost converter.

Equation (3) serves as the fundamental basis to traditional MPPT methodologies for determining the duty cycle of the converter during stable operating state. In an effort to enhance transient responses, it is vital for the MPPT to incorporate dynamic relationship between the $d(t)$ and v_{pv} . Transient oscillations pose a significant challenge to the efficient functioning of the system. Therefore, the MPPT technique must be designed to suppress these oscillations in the v_{pv} after updating the $d(t)$ to accommodate the changing weather conditions.^[24]

The equivalent small-signal circuit is considered to facilitate the transient response analysis of the solar PV system, as depicted in Figure 6. In which solar PV array is modeled a resistor R_{in} with small-signal array voltage (\hat{v}_{pv}) and current (\hat{i}_{pv}) across its terminal.

Apply KCL at node (a) in the Figure 6, where $\hat{d}(s)$ and $\hat{v}_{pv}(s)$ are the Laplace transform of $\hat{d}(t)$ and $\hat{v}_{pv}(t)$, respectively, we get

$$\frac{\hat{v}_{pv}(s)}{\hat{d}(s)} = \frac{-\frac{V_a}{LC_{in}}}{s^2 + \frac{1}{R_{in}C_{in}}s + \frac{1}{LC_{in}}} \quad (4)$$

The PV voltage is step up by decreasing the duty cycle, which is being proved by the minus sign in Equation (4). Due to the stochastic weather conditions, the system's driving point will fluctuate, consequently altering effective parameters in Equation (4), especially the R_{in} . In order to demonstrate the impact of R_{in} on the system, we shall proceed to analyze the denominator of Equation (4) in its canonical form.^[25] Where ξ is the damping ratio and ω_n denotes natural frequency.

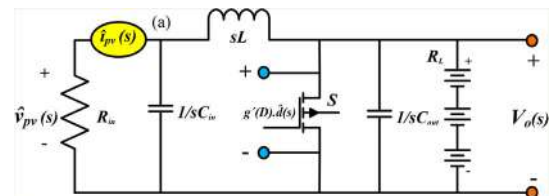


Figure 6. PV power conversion small-signal circuit diagram.

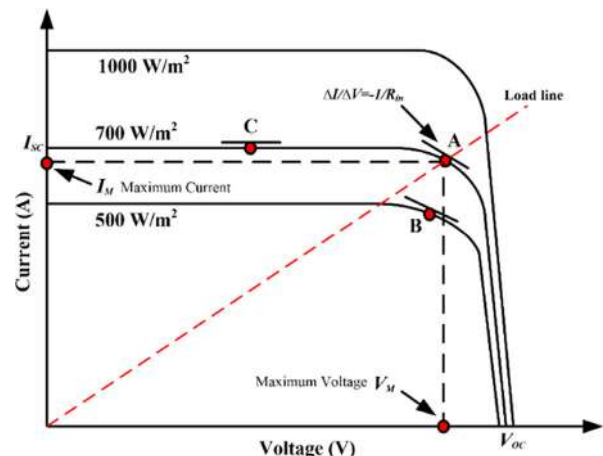


Figure 7. I-V characteristics with changing R_{in} .

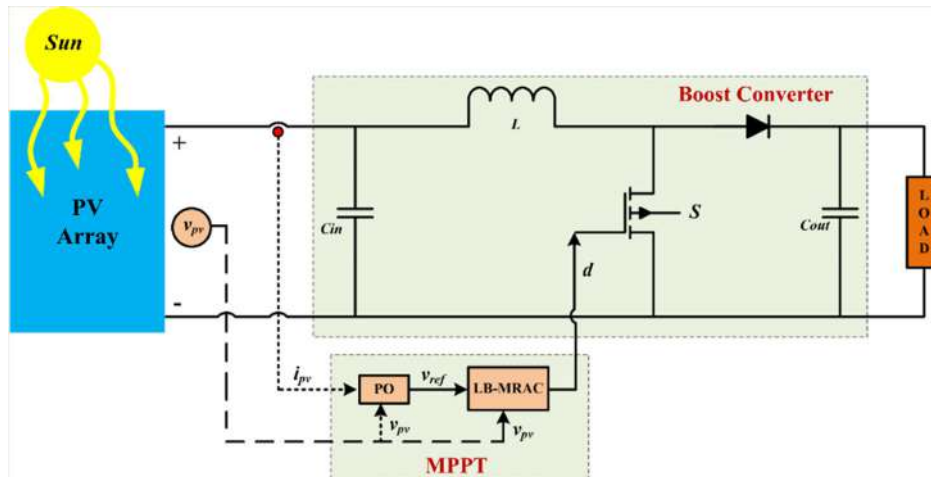


Figure 8. PV system with proposed MPPT architecture.

$$s^2 + 2\xi\omega_n s + \omega_n^2 = 0 \quad (5)$$

Calculating the value of ξ , after comparing Equation (4) and (5), we get

$$\xi = \frac{1}{2R_{in}} \sqrt{\frac{L}{C_{in}}} \quad (6)$$

For $\xi < 1$, the system exhibits underdamped behavior and displays oscillatory characteristics in its step response. The objective is to adjust the ξ of the regulated system to approximate 1, thereby achieving critical damping. Although R_{in} can be tuned to achieve critical damping for a specific operating point, a constant R_{in} cannot maintain critical damping across diverse operating conditions. **Figure 7** explains the I - V characteristic of solar PV panel having varied irradiance levels: 1000, 700, and 500 $W m^{-2}$. The determination of the R_{in} value for the PV array is achieved by analyzing the tangential slope at the operating point of the system.

$$\frac{1}{R_{in}} \approx -\frac{\Delta I}{\Delta V} \quad (7)$$

The point A denotes the MPP point (V_M, I_M) at irradiance 700 $W m^{-2}$. At the same irradiance level, whether operating point moves from A to C, then the R_{in} is also altered. Further, if it shifts from A to B, having different solar irradiance 500 $W m^{-2}$, again different R_i value will be obtained. Therefore, it cannot be guaranteed that the operating R_{in} will match the previous optimal R_{in} even at a new MPP. Furthermore, there is no assurance that the optimally running R_{in} will produce a critically damped response.^[26] Hence, an adaptive controller is designed using continuous-time LB-MRAC technique to regulate the converter dynamics and the operating point will be forced to the optimum R_{in} . So that, in spite of the stochastic weather, optimum R_{in} delivers the critically damped system such as $\xi = 1$.

3. Proposed MPPT Technique

The PV energy conversion system integrating proposed MPPT architecture is depicted in **Figure 8**. First of all, v_{pv} and i_{pv} are

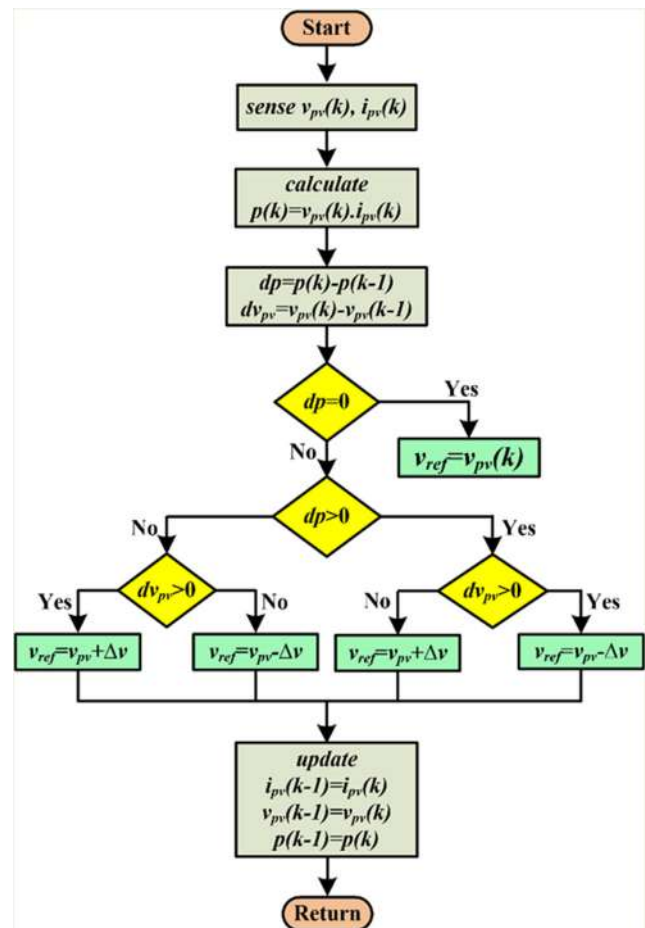


Figure 9. Flowchart for the reference voltage generation.

sensed by the PO technique and generate the reference voltage (v_{ref}) at each MPP. Next, the input to the continuous-time LB-MRAC is the difference between PV array and reference voltage. Finally, the MRAC provides a PWM duty cycle as the reference signal for the converter switch, to assure that the PV system is constantly working at MPP.

3.1. PO-Based Reference Voltage Generation

In the PO technique, the P–V curve of the solar panel plays a crucial role.^[27] The PO MPPT relies on the idea that the derivative of PV power vs voltage is zero at MPP, as explained in Equation (8). The v_{ref} is based on the control law as discussed in Equation (9). The flowchart for the reference voltage generation is shown in **Figure 9**, where Δv is the threshold voltage.

$$\frac{dp}{dv_{pv}} \begin{cases} > 0, \text{ at the left side of MPP} \\ = 0, \text{ at the MPP} \\ < 0, \text{ at the right side of MPP} \end{cases} \quad (8)$$

$$v_{ref} = \begin{cases} v_{pv}, \frac{dp}{dv_{pv}} = 0 \\ v_{pv} - \Delta v, \frac{dp}{dv_{pv}} < 0 \\ v_{pv} + \Delta v, \frac{dp}{dv_{pv}} > 0 \end{cases} \quad (9)$$

3.2. Lyapunov-Based MRAC Technique

The objective of MRAC is to build an adaptive technique that, regardless of deviation in the plant's characteristics or uncertainties, maintains the controlled plant's retaliation bordering on the reference model possessing the desired dynamics. This article

proposes the control rule for the second-order system and the expansion of the LB-MRAC from first to second order.^[28] The structure of the proposed continuous-time LB-MRAC method is illustrated in **Figure 10**. The system's input, $r(t)$, is the PO algorithm-calculated duty cycle change. The transfer function in Equation (4) matches Figure 10's plant model. To make sure that plant contains only positive terms, multiply to -1 . The output and input of plant are represented by $y_p(t)$ and $u_p(t)$, respectively.

The plant model is expressed as

$$\frac{d^2 y_p(t)}{dt^2} = -a_p \frac{dy_p(t)}{dt} - b_p y_p(t) + k_p u_p(t) \quad (10)$$

$$\frac{y_p(s)}{u_p(s)} = \frac{k_p}{s^2 + a_p s + b_p} \quad (11)$$

where k_p , a_p and b_p are determined using Equation (4). The reference model is selected, thus desired response is achieved by the $y_m(t)$ for (t).

$$\frac{d^2 y_m(t)}{dt^2} = -a_m \frac{dy_m(t)}{dt} - b_m y_m(t) + k_m r(t) \quad (12)$$

$$\frac{y_m(s)}{r(s)} = \frac{k_m}{s^2 + a_m s + b_m} \quad (13)$$

where $k_m > 0$, and a_m and b_m are chosen such as the reference model exhibits critically damped step response having bounded $r(t)$. The controller objective is to design $u_p(t)$, such that $y_p(t)$ asymptotically tracks $y_m(t)$.

$$u_p = \theta_1 r - \theta_2 \dot{y}_p - \theta_3 y_p = \theta^T \varphi \quad (14)$$

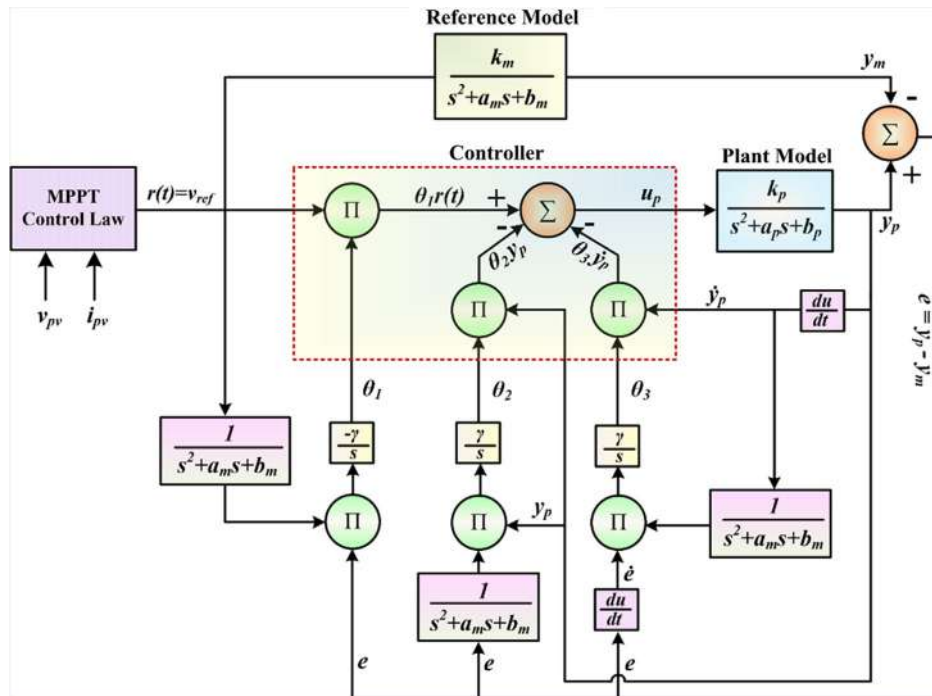


Figure 10. Architecture of the proposed continuous-time LB-MRAC method.

where $\theta = [\theta_1 \theta_2 \theta_3]^T$ is parameter estimation vector of the controller, and φ is specified as $[r \gamma_p \gamma_p]^T$. Now, replace the value of u_p in Equation (10), and we obtain

$$\frac{d^2 Y_p(t)}{dt^2} = -(a_p + k_p \theta_3) \frac{dY_p(t)}{dt} - (b_p + k_p \theta_2) Y_p(t) + k_p \theta_1 r(t) \quad (15)$$

After comparing Equation (12) and (15), we obtain

$$k_m = k_p \theta_1 \quad (16)$$

$$b_m = b_p + k_p \theta_2 \quad (17)$$

$$a_m = a_p + k_p \theta_3 \quad (18)$$

The control parameters θ_1 , θ_2 , and θ_3 can be converged as

$$\theta_1 \approx \frac{k_m}{k_p}; \theta_2 \approx \frac{b_m - b_p}{k_p}; \theta_3 \approx \frac{a_m - a_p}{k_p} \quad (19)$$

The error term is expressed as

$$e = Y_p - Y_m \quad (20)$$

Since the objective is to reduce e , it makes sense to infer the differential equation. Take the derivatives of Equation (20)

$$\frac{de}{dt} = \frac{dY_p}{dt} - \frac{dY_m}{dt} \quad (21)$$

$$\frac{d^2 e}{dt^2} = \frac{d^2 Y_p}{dt^2} - \frac{d^2 Y_m}{dt^2} \quad (22)$$

Now, substitute the value of $\frac{d^2 Y_p}{dt^2}$ and $\frac{d^2 Y_m}{dt^2}$ in the Equation (22)

$$\begin{aligned} \frac{d^2 e}{dt^2} = & \frac{dY_p}{dt} (-a_p - k_p \theta_3 + a_m) + Y_p (-b_p - k_p \theta_2 + b_m) \\ & + r(k_p \theta_1 - k_m) - a_m \frac{de}{dt} - b_m e \end{aligned} \quad (23)$$

The $e(t)$ is zero, if parameters have equal value in Equation (19). Hence, a parameter adjustment mechanism is devised to get the desired value of θ_1 , θ_2 , and θ_3 . The Lyapunov stability theorem states that, if a scalar function $V(t)$ exists, which is real, continuous and also the continuous first partial derivatives through $\dot{V}(t) < 0$ for all $t \neq 0$, such type of system is stable asymptotically. Suppose $k_p \gamma > 0$, and then Lyapunov function V is defined as

$$\begin{aligned} V(e, \dot{e}, \theta_1, \theta_2, \theta_3) = & \frac{1}{2} \frac{(a_p + k_p \theta_3 - a_m)^2}{\gamma k_p} + \frac{1}{2} \frac{(b_p + k_p \theta_2 - b_m)^2}{\gamma k_p} \\ & + \frac{1}{2} \frac{(k_p \theta_1 - k_m)^2}{\gamma k_p} + \frac{1}{2} \left(\frac{de}{dt} \right)^2 + \frac{1}{2} b_m e^2 \end{aligned} \quad (24)$$

As $e = 0$, then also $V = 0$ and in this condition, the desired value of θ_1 , θ_2 , and θ_3 is obtained. When $\frac{dV}{dt} < 0$, then the function is the Lyapunov.

$$\begin{aligned} \frac{dV}{dt} = & \frac{(a_p + k_p \theta_3 - a_m)}{\gamma} \left(\frac{d\theta_3}{dt} - \dot{e} \gamma_p \right) \\ & + \frac{(b_p + k_p \theta_2 - b_m)}{\gamma} \left(\frac{d\theta_2}{dt} - \dot{e} \gamma_p \right) \\ & + \frac{(k_p \theta_1 - k_m)}{\gamma} \left(\frac{d\theta_1}{dt} + \dot{e} r \right) - a_m \dot{e}^2 \end{aligned} \quad (25)$$

Now the adaptation rule is given as

$$\frac{d\theta_1}{dt} = -\gamma r \dot{e} \quad (26)$$

Table 1. Simulation specifications.

Parameter	Value	Parameter	Value
Rated voltage $[V_M]$	29 V	Inductor $[L]$	3.8 mH
Rated current $[I_M]$	7.35 A	Input capacitor $[C_{in}]$	113.83 μ F
Rated power $[P_M]$	213.15 W	Output capacitor $[C_{out}]$	113.83 μ F
Open circuit voltage $[V_{oc}]$	36.3 V	Load $[R_L]$	20 Ω
Short circuit current $[I_{sc}]$	7.84 A	$a_p = 1/R_{in} \times C_{in}$	351 $[\text{rad s}^{-1}]$
Parallel resistance $[R_p]$	313.399 Ω	$b_p = 1/L \times C_{in}$	$2.30 \times 10^6 [(\text{rad s}^{-1})^2]$
Series resistance $[R_s]$	0.3938 Ω	$k_p = V_o/L \times C_{in}$	$2.95 \times 10^8 \text{ V } [(\text{rad s}^{-1})^2]$
Cells per module	60	a_m	$3.02 \times 10^3 [\text{rad s}^{-1}]$
No. of series modules	2	b_m	$2.30 \times 10^6 [(\text{rad s}^{-1})^2]$
No. of parallel modules	2	k_m	$2.95 \times 10^8 \text{ V } [(\text{rad s}^{-1})^2]$
R_{in}	25 Ω	Adaption gain $[\gamma]$	0.08
Switching frequency $[f_s]$	20 kHz	Simulation step time $[T_s]$	1 μ s

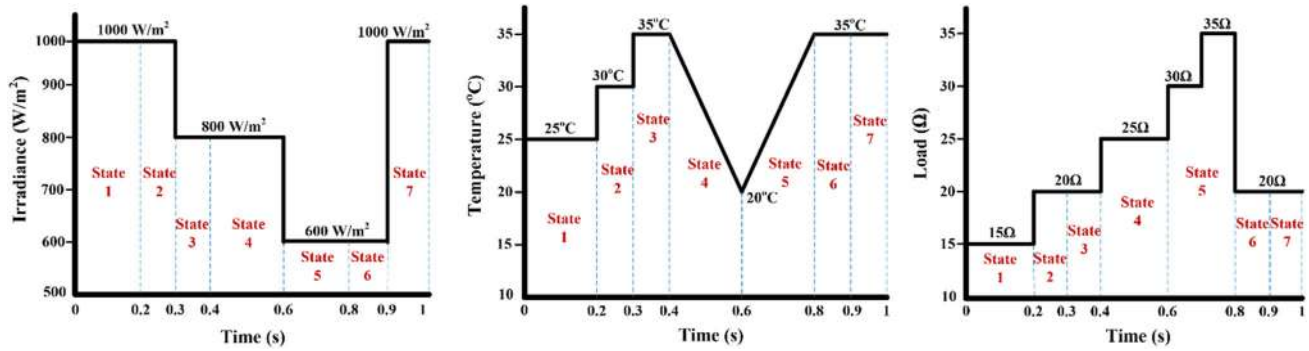


Figure 11. Stochastic irradiance, temperature, and load profiles.

$$\frac{d\theta_2}{dt} = \gamma \gamma_p \dot{e} \quad (27)$$

$$\frac{d\theta_3}{dt} = \gamma \gamma_p \dot{e} \quad (28)$$

So, the Lyapunov function is expressed as

$$\frac{dV}{dt} = -a_m \dot{e}^2 \quad (29)$$

As a result, rather than being negative definite, the time derivative of V is semidefinite (negative). Hence, it is implied that $V(t) \leq V(0)$, and therefore, $\theta_1, \theta_2, \theta_3, e$, and \dot{e} must be bounded. It is concluded that $\gamma_p = e + \gamma_m$ is also bounded. Derivative of Equation (29) provides the vital condition to confirm that \dot{V} is bounded.

$$\frac{d^2V}{dt^2} = -2a_m \dot{e} \frac{d\dot{e}}{dt} \quad (30)$$

Now, put the value of $\frac{d\dot{e}}{dt}$ in Equation (30), we get

$$\frac{d^2V}{dt^2} = -2a_m \dot{e} \left\{ \begin{array}{l} -\frac{d\gamma_p}{dt} (a_p + k_p \theta_3 - a_m) - \gamma_p (b_p + k_p \theta_2 - b_m) + r (k_p \theta_1 - k_m) \\ -a_m \frac{d\dot{e}}{dt} - b_m \dot{e} \end{array} \right\} \quad (31)$$

Since r, γ_p , and e are bounded, then \dot{V} is also bounded. Consequently, $\frac{dV}{dt}$ is uniformly continuous. The design of the proposed continuous-time Lyapunov-based MRAC scheme for MPPT application is realized.

4. Simulation Results and Discussion

The primary parts of the suggested system design: selection of PV panel; converter modeling; development of novel continuous-time LB-MRAC technique. The simulation is carried out through the MATLAB/Simulink software. The simulation specifications employed to design proposed system are given in Table 1. The performance of the suggested LB-MRAC technique is demonstrated under stochastic weather scenarios through different testing modes as discussed in the subsequent sections.

The comparative study of the proposed LB-MRAC with the cutting-edge MPPT techniques, such as PO, INC, and ANFIS, is verified in each mode. The MPPT schemes tracking and overall efficiency (η) are determined as

$$\eta_{\text{tracking}} = \frac{\int_{t_1}^{t_2} p_{\text{avg}} dt}{\int_{t_1}^{t_2} p_M dt} \quad (32)$$

$$\eta_{\text{overall}} = \frac{p_{\text{out}}}{p_M} \quad (33)$$

The algorithm starts tracing at t_1 , while it finishes at t_2 . The average power produced between t_1 and t_2 is denoted by p_{avg} . The

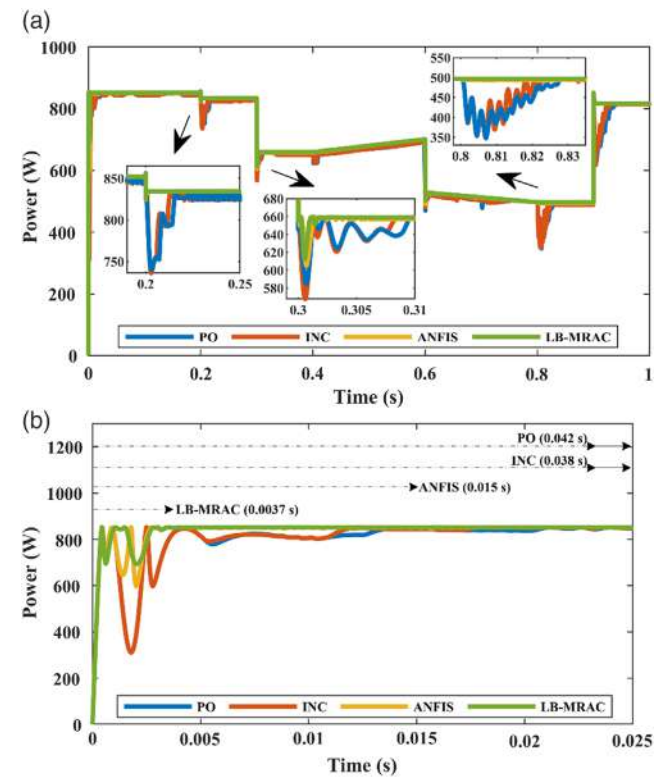


Figure 12. Under stochastic weather with load uncertainties a) PV power, b) tracking speed (state 1).

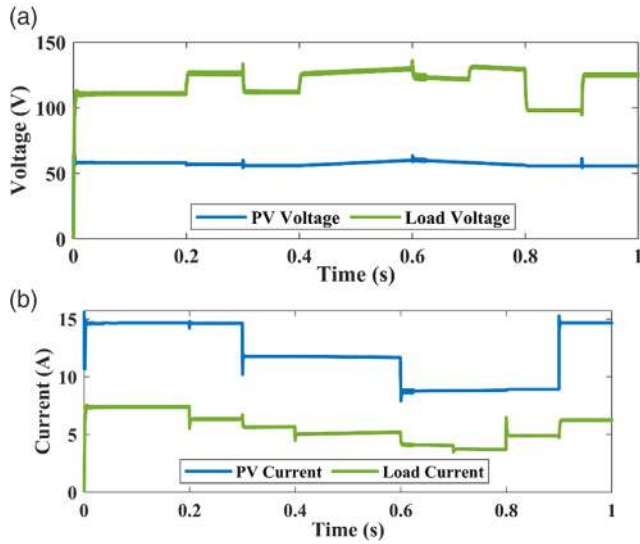


Figure 13. a) PV voltage vs. load voltage, b) PV current vs. load current.

p_{out} is the average power output, and the p_M stands for nominal maximum power reachable.

4.1. Standalone Mode: Highly Fluctuating Weather Conditions with Load Uncertainties

Stochastic irradiance, temperature, and load signals are represented in **Figure 11**. Seven different states (S1–S7) are considered in each signal. In order to generate the unexpected disturbance into the system, load uncertainties are considered with the stochastic weather conditions.

Figure 12a depicts the PV power under stochastic weather with load uncertainties. **Figure 12b** explains the tracking speed in the state 1, i.e., within 3.7 ms, the proposed LB-MRAC technique tracks MPP, while ANFIS takes 15 ms, INC takes 38 ms, and PO takes 42 ms. **Figure 13a,b** illustrates the PV voltage vs. load voltage and PV current vs. load current, respectively.

Table 2 incorporates the detailed comparative analysis in seven stochastic weather states. It is analyzed that within milliseconds, the proposed LB-MRAC MPPT tracks MPP in all states. Consequently, the tracking efficiency (i.e., more than 99%) is highest among cutting-edge techniques. The average actual power of the LB-MRAC MPPT is close to maximum power as well as the overall efficiency of the proposed system is more than 98%, which is impressive.

Table 2. Detailed comparative analysis in seven stochastic weather states.

MPPT techniques	S1	S2	S3	S4	S5	S6	S7
	0–0.2 s	0.2–0.3 s	0.3–0.4 s	0.4–0.6 s	0.6–0.8 s	0.8–0.9 s	0.9–1 s
Tracking time [s]							
PO	0.042	0.048	0.054	0.058	0.058	0.054	0.062
INC	0.038	0.045	0.040	0.045	0.052	0.036	0.055
ANFIS	0.015	0.014	0.012	0.014	0.016	0.011	0.012
LB-MRAC	0.0037	0.0039	0.0048	0.0058	0.0069	0.005	0.0041
Tracking efficiency [%]							
PO	93.38	94.46	94.17	94.47	94.83	94.19	94.31
INC	94.46	95.32	95.33	95.56	96.11	96.08	94.95
ANFIS	98.24	97.89	98.25	98.49	98.16	98.11	97.93
LB-MRAC	99.15	99.37	99.59	99.51	99.53	99.22	99.25
Average actual power [W]							
PO	810.5	812	648.6	645.1	484.5	487	789.3
INC	814	816.3	650.8	649.7	486	488.4	793
ANFIS	832.4	830.8	668.1	670	498	498.6	824.7
LB-MRAC	846	846.5	675.8	676.3	505.3	505.8	839.4
Average power output [W]							
PO	781	785.38	627.55	628.35	469.54	471	775.52
INC	781.53	789.31	630	633.45	469.60	471.86	778.27
ANFIS	828.56	829.76	662	661.2	493.15	493.31	811.53
LB-MRAC	838.26	840.3	672.4	670.5	503.11	504.49	837.52
Overall efficiency [%]							
PO	91.66	92.18	92.07	92.18	91.85	92.13	91.02
INC	91.72	92.64	92.42	92.93	91.86	92.30	91.34
ANFIS	97.24	97.38	97.12	97	96.46	96.50	95.25
LB-MRAC	98.38	98.62	98.65	98.37	98.41	98.68	98.30

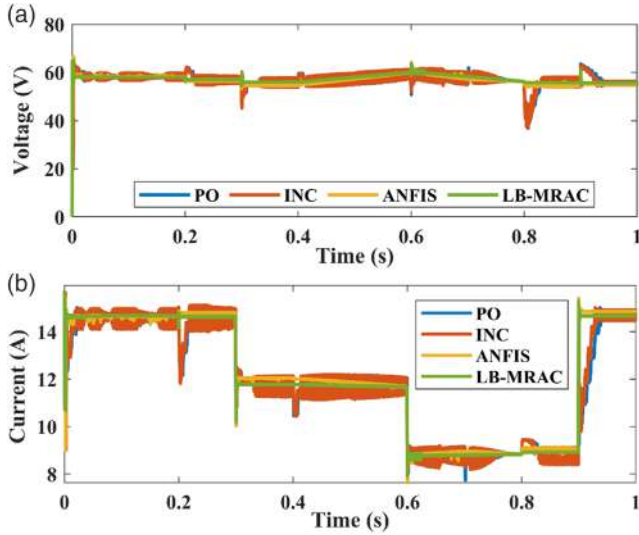


Figure 14. a) PV voltage, b) PV current.

Figure 14a,b depicts the PV voltage and current of all four techniques, respectively. These results certainly evidence that suggested LB-MRAC MPPT has least voltage and current ripples, which are useful metrics to compare the system performance. The voltage and current ripple charts for each state are exhibited in Figure 15a,b, correspondingly. It is obvious that the suggested algorithm has negligible ripple compared to ANFIS, INC, and PO MPPT algorithms, which have noticeable ripples.

Figure 16 analyses the power loss in all seven states. Equation (34), where t is the amount of time needed to arrive at MPP, is used to calculate it.^[20] According to findings, the proposed MPPT strategy has negligible power loss in stochastic weather conditions.

$$\text{Power loss} = \frac{\sum p_M(t) - \sum p(t)}{\sum p_M(t)} \times 100\% \quad (34)$$

4.2. Partial Shading Mode: Diverse Shading Patterns

In the partial shading mode, three PV panels are linked in series to produce a maximum output of 1.05 kW. Patterns 1, 2, 3, and 4

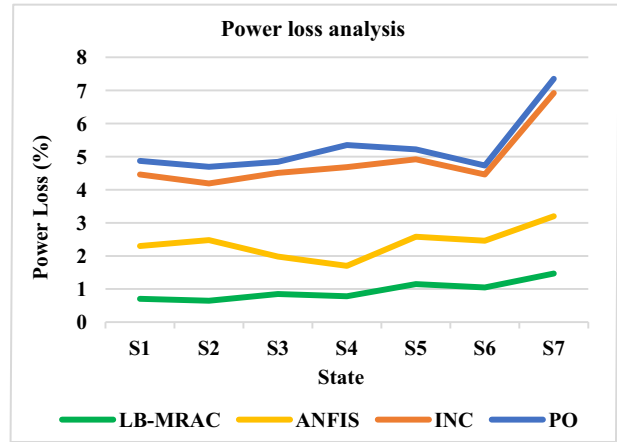
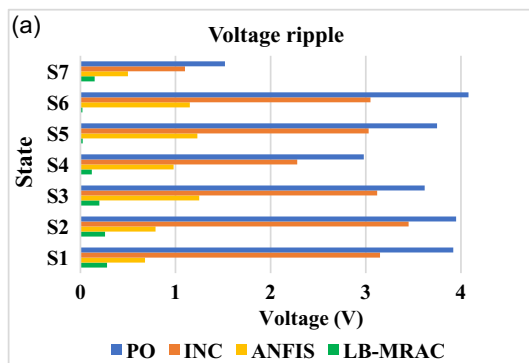


Figure 16. Power loss analysis in all seven states.

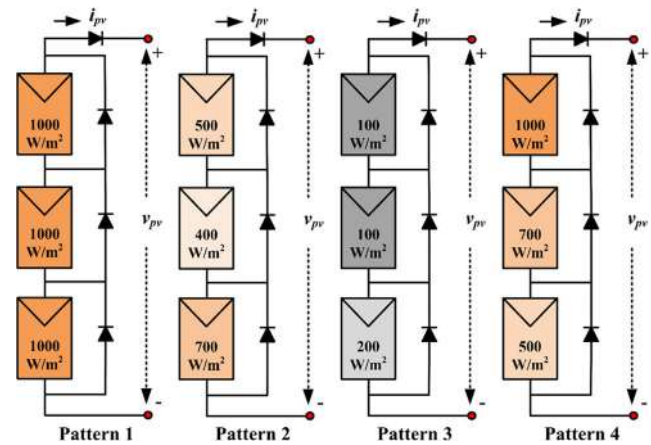


Figure 17. Diverse shading patterns.

(i.e., P1, P2, P3, and P4) are examples of diverse shading generated by the PV panels when they are activated at various radiation levels, as seen in Figure 17. The proposed continuous-time LB-MRAC is evaluated against ANFIS, INC, and PO concerning shading loss, tracked power, and GMPP tracking time. Shading loss, i.e., given in Equation (35), is the power loss caused by shading.^[29]

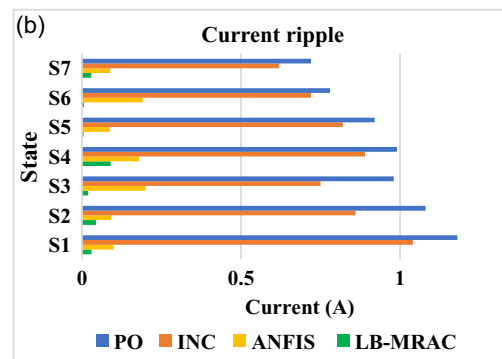


Figure 15. a) PV voltage ripple chart, b) PV current ripple chart.

$$\text{Shading loss} = p_{M(\text{without shading})} - p_{M(\text{shading})} \quad (35) \quad 4.2.2. \text{ Pattern 2}$$

The P-V curve is depicted in **Figure 18a**, and the PV power of the suggested LB-MRAC, ANFIS, INC, and PO approaches is shown in **Figure 18b** under diverse shading scenarios.

4.2.1. Pattern 1

The suggested LB-MRAC tracks maximum power of 997.70 W having minimal oscillations close to GMPP as well as shading loss of only 51.3 W. The PO algorithm has maximum shading loss of 209.67 W and tracks 839.33 W, whereas INC and ANFIS track 843 and 932.03 W, respectively.

In this pattern, the PO, INC, and ANFIS track 333.30, 337.4, and 410.38 W, and their shading losses are 715.7, 711.6, and 638.62 W, respectively. The proposed LB-MRAC harvests 448.60 W and shading loss of 600.4 W, which is minimum.

4.2.3. Pattern 3

The LB-MRAC technique harvests maximum power of 113.09 W and exhibits trivial fluctuations around GMPP with minimal shading loss of 935.91 W. The PO, INC, and ANFIS trace only 42.63, 59.78, and 77.85 W and similarly their shading losses occur 1006.37, 989.22, and 971.15 W.

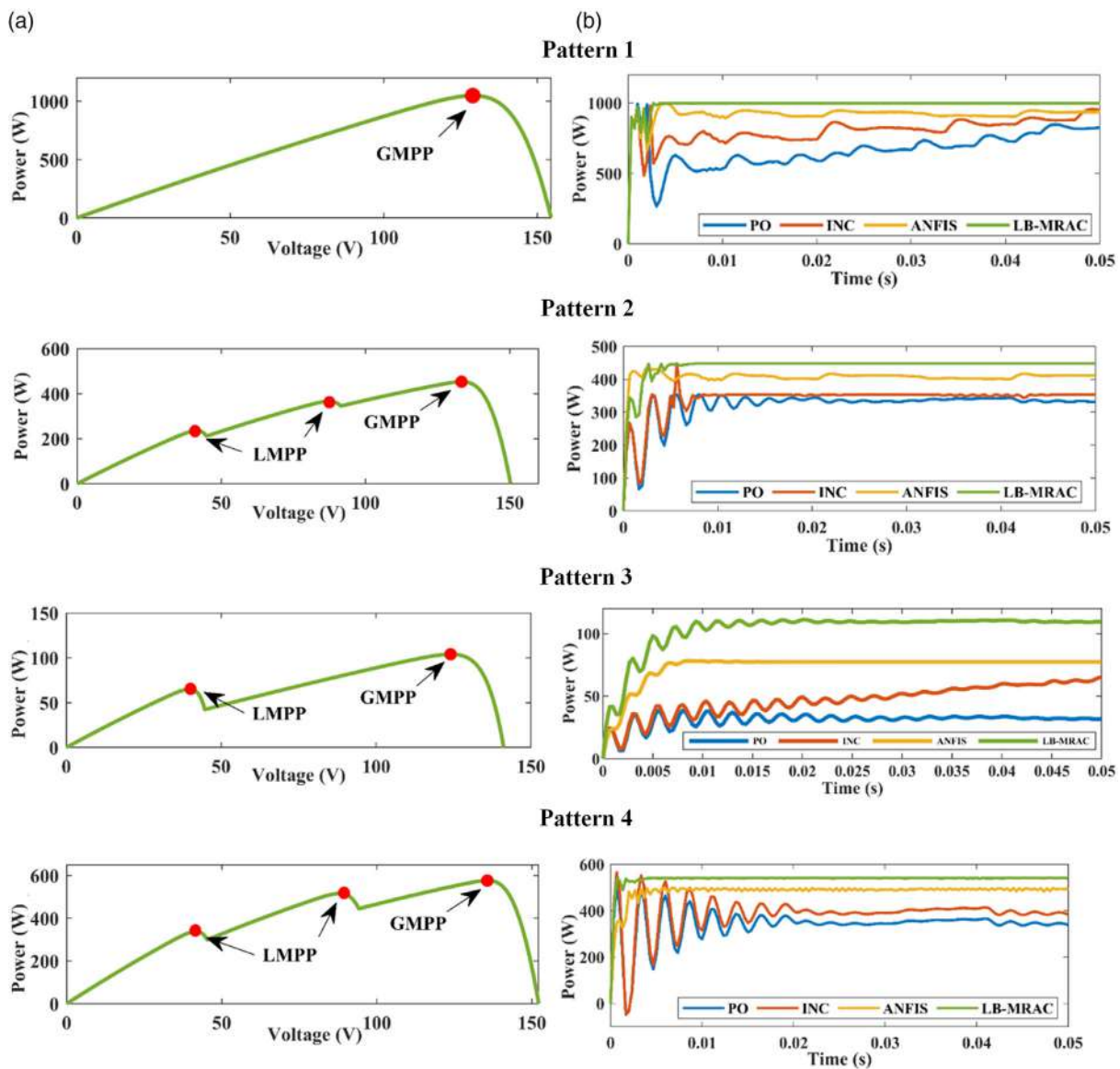


Figure 18. a) P-V characteristics, b) PV power for all shading patterns.

4.2.4. Pattern 4

In the pattern, LB-MRAC MPPT traces 554.81 W without oscillation at GMPP and has shading loss of 494.19 W. The ANFIS detects 493.17 W, INC tracks 341.48 W, whereas PO traces only 338.64 W, rendering it least efficient as of maximum shading loss 710.36 W.

Table 3 provides a thorough comparison of all shading patterns under PSC with LMPP as well as GMPP. It is analyzed that the suggested LB-MRAC method catches the highest power and has the minimum shading losses under each circumstance. The PO and INC approach gather the least power besides the most shading losses in each pattern. Figure 19 and 20 demonstrate, respectively, the tracked power as well as shading losses for the cutting-edge methods used in each pattern.

Table 3. Comparative analysis of different methods under PSC.

Pattern	Method	Power [W]	Voltage [V]	Current [A]
Pattern 1:	PO	839.33	112.06	7.49
GMPP: 1049 W	INC	843	112.40	7.50
	ANFIS	932.03	114.5	8.14
	LB-MRAC	997.70	119.20	8.37
Pattern 2:	PO	333.30	68.02	4.90
GMPP: 453.3 W	INC	337.4	68.30	4.94
LMPP: 366.1, 236 W	ANFIS	410.38	82.24	4.99
	LB-MRAC	448.60	82.92	5.41
Pattern 3:	PO	42.63	26.32	1.62
GMPP: 124.1 W	INC	59.78	32.14	1.86
LMPP: 65 W	ANFIS	77.85	39.52	1.97
	LB-MRAC	113.09	57.12	1.98
Pattern 4:	PO	338.64	39.24	8.63
GMPP: 576.4 W	INC	341.48	39.25	8.70
LMPP: 516.5, 338.2 W	ANFIS	493.17	58.85	8.38
	LB-MRAC	554.81	63.48	8.74

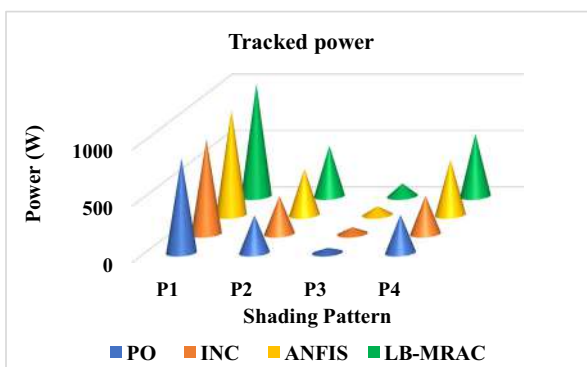


Figure 19. Tracked power under each pattern.

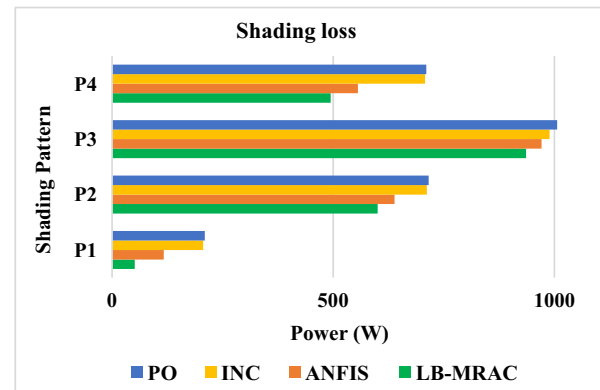


Figure 20. Shading losses under each pattern.

4.3. Grid-Integration Mode: Realistic Weather

The majority of grid-integrated systems are aimed to maximize power supply to grid by boosting operation of the PV system under stochastic weather conditions. Grid-connected systems must perform two critical tasks in order to reach this objective: 1) Guarantee that the solar PV system is functioning at MPP utilizing MPPT technique and 2) successfully interject grid current, i.e., free of harmonic distortion.^[30,31]

Even if, total harmonic distortion (THD) is below the IEEE 519 benchmark, whose limit is 5%, the grid-injected currents contain substantial harmonic content. It is evident that the most relevant harmonic components in the grid-injected currents of the 5th, 7th, 11th, and 13th orders of the fundamental component. Additional control actions are integrated in the controller to deal with these harmonic contents. Furthermore, the implemented harmonic compensation technique can be expanded to any desired component. However, the complexity of the system must be taken into consideration.^[32]

In the grid-integrated mode, the functioning of the continuous-time LB-MRAC approach is examined through realistic weather conditions. The schematic representation of the grid-integrated solar PV system is explained in Figure 21, and parameters used to design such system are detailed in Table 4. The main parts of this system are PV module, boost converter, an inverter, grid, and load.

The grid-integrated validation of the proposed LB-MRAC technique using realistic weather conditions is demonstrated in Figure 22a. It is evident that the suggested system precisely and almost oscillation-free tracks the ideal power. The injected grid voltage and current are also showed in Figure 22b,c, respectively, both exhibit the correct synchronization and efficacy of the proposed technique.

Through FFT analysis, the THD calculation is also performed, and it results in that the grid current has 2.71%, which follow IEEE 519 benchmark maximum THD limit of 5%. Figure 22d explains the THD analysis of the grid current. It is observed the most relevant harmonic components in the grid-injected currents of the 5th (250 Hz), 7th (350 Hz), 11th (550 Hz), and 13th (650 Hz) orders of the fundamental component.

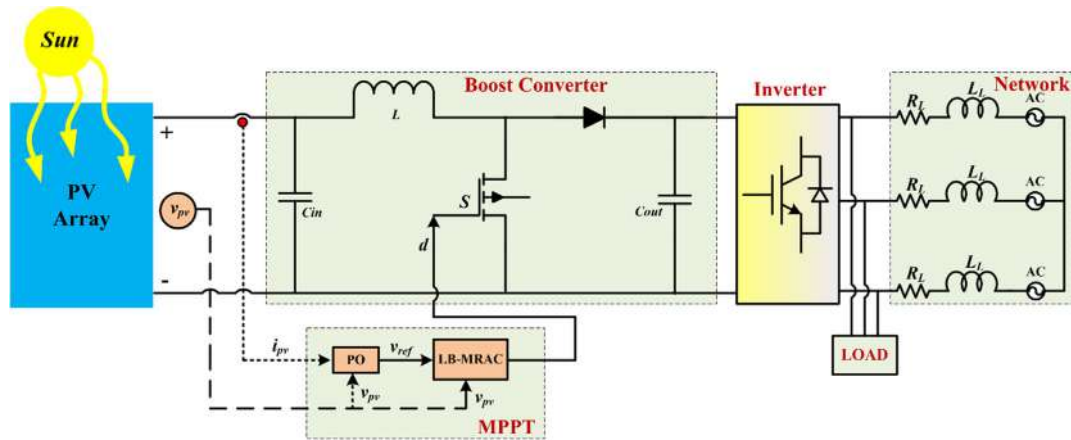


Figure 21. Schematic representation of grid-integrated proposed system.

Table 4. Grid-Integrated simulation specifications.

Parameter	Value	Parameter	Value
PV panel [14 series and 17 parallel]	213.15 W and 29 V	Filter inductance [per phase]	2.8 mH
Nominal power	50 kW	Inductor resistance	0.7 Ω
Grid voltage	380 V	Grid frequency	50 Hz
Capacitance [DC link]	330 μ F	Sampling time	10 μ s

5. Real-Time Mode: Experimental Validation Using OPAL-RT (OP4510)

In this mode, the real-time conformity of the proposed continuous-time LB-MRAC MPPT is validated as shown in **Figure 23**. Real-time simulators are intended to produce proposed system results under real electrical environment, like as real-time hardware. For interacting in the real time, the OP4510 has a four-core processor, 32 Digital I/O channels, a Kintex-7 FPGA, and 16 analog I/O channels. The high switching frequency operation, including PWM generating circuits of the converters, is ideally suited for Kintex-7 FPGA employed in the OPAL-RT.^[33]

The OP4510 utilizes RT-Lab to interface the Simulink model placed in host PC with the simulator in order to deliver real-time results. By converting the test model into executable code, the RT-Lab facilitates connection between Simulink model of the proposed system produced in the host PC and the OPAL-RT. The OP4510's CPU then executes this code and produces results in real time using digital oscilloscope. The sampling time is chosen 20 μ s to ensure the compatibility between simulator and MATLAB/Simulink model. The performance of the suggested LB-MRAC technique is corroborated under different testing conditions, including standalone and grid-integrated mode at varying irradiance levels.

5.1. Real-Time Validation Under Standalone Mode

In standalone mode, the performance of the PO and INC MPPT varying irradiance level from 1000 to 500 W m^{-2} , and the effect

on the power, voltage, and current is presented in **Figure 24a**. The performance of the ANFIS MPPT in real time is demonstrated in **Figure 24b** under varying irradiance level from 600 to 800 W m^{-2} . The real-time result for the proposed LB-MRAC technique is illustrated in **Figure 24c** varying irradiance level from 1000 to 500 W m^{-2} .

The oscillation in the steady state for the PO and INC MPPT is very high and almost similar response under varying irradiance level, whereas ANFIS has less oscillation near MPP but it exists. It is evident that LB-MRAC MPPT exhibits good performance under varying irradiance level and negligible oscillation near MPP.

5.2. Real-Time Validation Under Grid-Integrated Mode

In grid-integrated mode, the effectiveness of the suggested continuous-time LB-MRAC method under varying irradiance level, including low (500 W m^{-2}) to high (700 W m^{-2}) and high to low, is shown in **Figure 25a,b** correspondingly. The effect on the power, grid voltage, and current is shown in the respective figures. It is analyzed that efficient and precise tracking of the PV power employing LB-MRAC technique under stochastic weather conditions. The grid voltage and current are in sinusoidal alignment to each other.

The comparative study of the suggested continuous-time LB-MRAC technique with the state-of-the-art MPPT is accomplished with the help of radar chart considering six performance evaluation parameters, including tracking speed, steady-state oscillation, efficiency, complexity, capability in PSC, and Grid

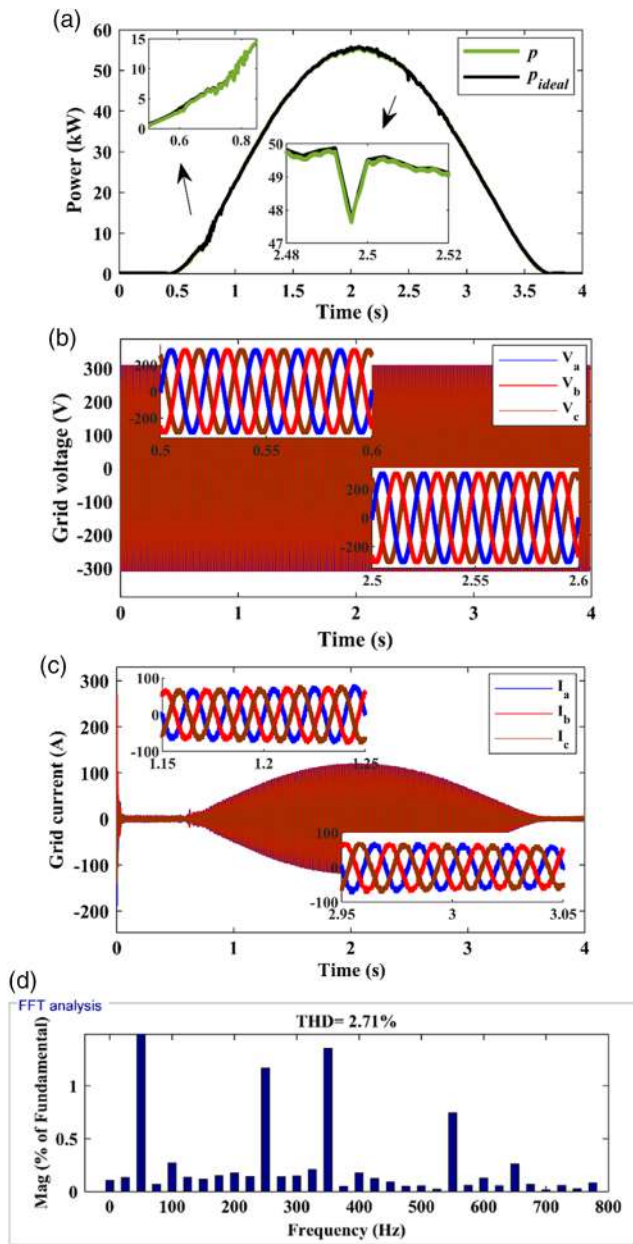


Figure 22. Grid-integrated validation using LB-MRAC technique a) The PV and ideal power b) Grid voltage c) Grid current d) THD analysis of the grid current.

integration, as depicted in **Figure 26**. The radar chart contour is normalized from 4 (maximum) to 1 (minimum). The strength and weakness of each technique are plotted on the maximum and minimum scale of the radar chart, respectively. In the spider diagram, the broad contour area surmounts the narrow region.

Tracking speed is categorized into four distinct categories such as very fast (0.001–0.01 s), fast (0.01–0.1 s), medium

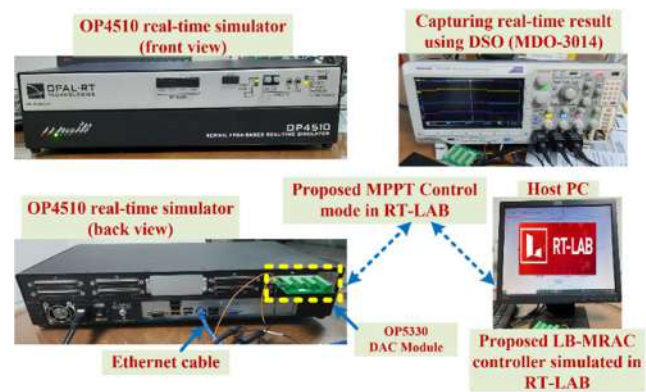


Figure 23. Experimental setup to validate proposed continuous-time LB-MRAC technique.

(0.1–1 s), and slow (more than 1 s). Efficiency is categorized into four categories such as very high (more than 99.50%), high (99–99.5%), medium (98–99%), and low (less than 98%). In the similar way, complexity and steady-state oscillation are also categorized. For the PSC and grid-integration, radar plots are either minimum (1) or maximum (4) depending upon the method validation.

It is evident that the recommended LB-MRAC approach is dominant among state-of-the-art techniques regarding tracking speed, efficiency, complexity, steady-state oscillations, capability to operate under PSC, and grid-integrated mode.

6. Conclusion

A novel continuous-time LB-MRAC scheme is designed and implemented for the MPPT application under stochastic weather circumstances. This technique is the best choice for the time-bounded nonlinear MPPT problem among the compared techniques. The effectiveness of the suggested LB-MRAC is compared to cutting-edge techniques such as ANFIS, INC, and PO in each mode. In standalone mode, under highly fluctuating irradiance and temperature with load uncertainties, the tracking time to reach MPP for the suggested LB-MRAC MPPT is only 3.7 ms, whereas ANFIS, INC, and PO take 15, 38, and 42 ms, respectively. The tracking efficacy of the LB-MRAC lies between 99.15% and 99.59%, and its overall efficiency is more than 98%, i.e., highest among all state-of-the-art techniques. At 1000 W m^{-2} , the average power tracked by the LB-MRAC technique is 846 W with minimal oscillations, whereas ANFIS, INC, and PO track only 831, 816, and 812 W, respectively. The proposed technique has negligible voltage and current ripples as well as minimum power loss in all seven states. In partial shading mode, the recommended MPPT approach is competent to locate and track the GMPP with minimal oscillations, despite variations in shading patterns. It takes only 0.04 s to trace GMPP, with minimal shading loss in each pattern such as P1, P2, P3,

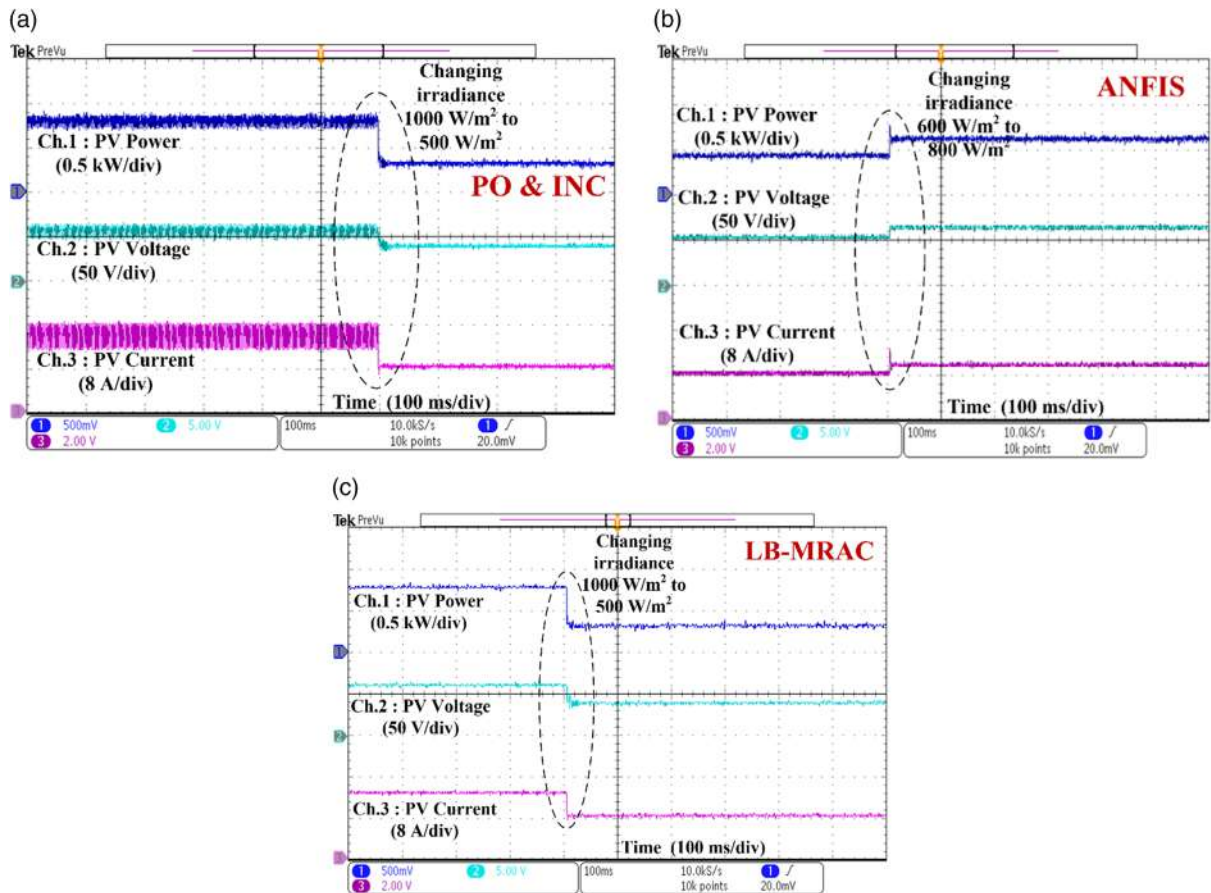


Figure 24. Real-time validation under standalone a) PO and INC, b) ANFIS, and c) proposed LB-MRAC technique.

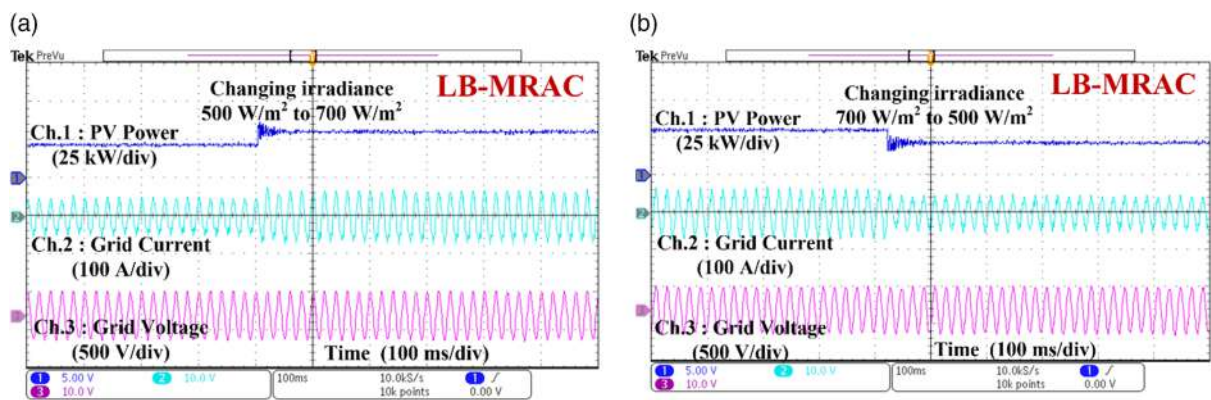


Figure 25. Real-time validation under grid-integrated mode a) low to high irradiance level and b) high to low irradiance level.

and P4. In grid-integrated mode, a 50-kW test system is designed, and the continuous-time LB-MRAC technique effectively tracks MPP in realistic weather conditions. The injected grid current satisfies the IEEE 519 benchmark. Eventually,

real-time experimental corroboration using OPAL-RT(OP4510) is demonstrated, and it confirms the feasibility and efficacy of the proposed continuous-time LB-MRAC² technique in the real world.

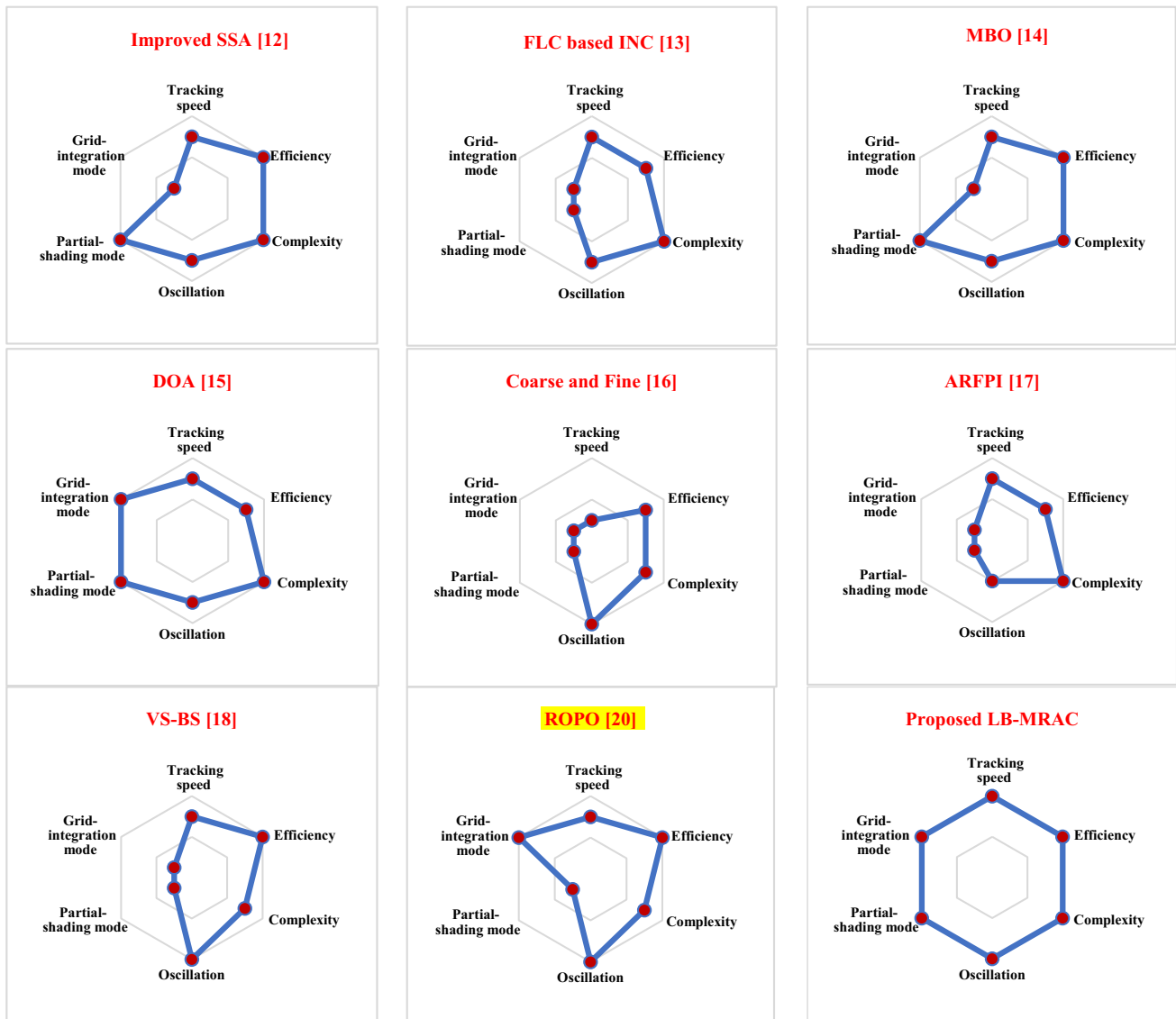


Figure 26. Performance comparison of the suggested LB-MRAC with state-of-the-art MPPT methods using radar charts.

Conflict of Interest

The authors declare no conflict of interest.

Received: July 11, 2023
Revised: November 1, 2023
Published online:

Data Availability Statement

The data that support the findings of this study are available from the corresponding author upon reasonable request.

Keywords

grid integrated, Lyapunov-based model reference adaptive control, OPAL-RT(OP4510), partial shading, solar energy conversion technology, stand-alone

- [1] D. K. Singh, A. K. Akella, S. Manna, *Environ. Prog. Sustainable Energy* **2022**, *41*, 1.
- [2] Renewable Capacity Statistics 2023, <https://www.google.com/search?q=Renewable+capacity+statistics+2023> (accessed: June 2023).
- [3] M. S. Wasim, M. Amjad, S. Habib, M. A. Abbasi, A. R. Bhatti, S. M. Mueen, *Energy Rep.* **2022**, *8*, 4871.
- [4] R. B. Bollipo, S. Mikkili, P. K. Bonthagorla, *CSEE J. Power Energy Syst.* **2021**, *7*, 9.
- [5] P. K. Pathak, A. K. Yadav, P. A. Alvi, *Neural Comput. Appl.* **2022**, *34*, 171.
- [6] S. Manna, A. K. Akella, D. K. Singh, *Iran. J. Sci. Technol.* **2023**, *47*, 233.

- [7] K. H. Chao, Y. S. Lin, U. D. Lai, *Appl. Energy* **2015**, *158*, 609.
- [8] P. Srinivasarao, K. Peddakapu, M. R. Mohamed, K. K. Deepika, K. Sudhakar, *Comput. Electr. Eng.* **2021**, *89*, <https://doi.org/10.1016/j.compeleceng.2020.106910>.
- [9] H. Aminnejhad, S. Kazemina, M. Aliasghary, *Optik* **2021**, *247*, <https://doi.org/10.1016/j.ijleo.2021.167983>.
- [10] J. Aguila-Leon, C. Vargas-Salgado, C. Chiñas-Palacios, D. Díaz-Bello, *Expert Syst. Appl.* **2023**, *211*, <https://doi.org/10.1016/j.eswa.2022.118700>.
- [11] S. Pei Ye, Y. Hua Liu, S. Chung Wang, H. Yu Pai, *Appl. Energy* **2022**, *321*, <https://doi.org/10.1016/j.apenergy.2022.119380>.
- [12] D. Fares, M. Fathi, I. Shams, S. Mekhilef, *Energy Convers. Manage.* **2021**, *230*, <https://doi.org/10.1016/j.enconman.2020.113773>.
- [13] N. Bouarroudj, B. Benlahbib, Y. Houama, M. Sedraoui, V. F. Batlled, T. Abdelkrima, D. Boukhetalae, F. Boudjema, *Energy Sources, Part A* **2021**, <https://doi.org/10.1080/15567036.2021.1955049>.
- [14] I. Shams, S. Mekhilef, K. S. Tey, *IEEE Trans. Power Electron.* **2021**, *36*, 5569.
- [15] E. Lodhi, F.-Y. Wang, G. Xiong, G. A. Mallah, M. Y. Javed, T. S. Tamir, D. W. Gao, *Sustainability* **2021**, *13*, 1.
- [16] M. Kavya, S. Jayalalitha, *ISA Trans.* **2022**, *121*, 180.
- [17] V. Kumar, A. Mitra, O. Shaklya, S. Sharma, K. P. S. Rana, *Optik* **2022**, *259*, <https://doi.org/10.1016/j.ijleo.2022.168942>.
- [18] A. Charaabi, A. Zaidi, O. Barambones, N. Zanzouri, *Int. J. Electr. Power Energy Syst.* **2022**, *136*, <https://doi.org/10.1016/j.ijepes.2021.107682>.
- [19] Z. M. Ali, T. Alquthami, S. Alkhalaf, H. Norouzi, S. Dadfar, K. Suzuki, *Sustain. Energy Technol. Assess.* **2022**, *52*, <https://doi.org/10.1016/j.seta.2022.102156>.
- [20] P. K. Pathak, A. K. Yadav, P. A. Alvi, *J. Eng. Res.* **2022**, *11*, 112.
- [21] N. Priyadarshi, S. Padmanaban, J. B. Holm-Nielsen, F. Blaabjerg, M. S. Bhaskar, *IEEE Syst. J.* **2020**, *14*, 1218.
- [22] L. V. Bellinaso, H. H. Figueira, M. F. Basquera, R. P. Vieira, H. A. Grundling, L. Michels, *IEEE Trans. Ind. Appl.* **2019**, *55*, 1903.
- [23] R. Dadkhah Tehrani, F. Shabaninia, *Trans. Inst. Meas. Control* **2018**, *40*, 3709.
- [24] A. Tavakoli, M. Forouzanfar, *Int. Trans. Electr. Energy Syst.* **2020**, *30*, <https://doi.org/10.1002/2050-7038.12753>.
- [25] L. Nousiainen, J. Puukko, A. Mäki, T. Messo, J. Huusari, J. Jokipii, J. Viinamäki, D. T. Lobera, S. Valkealahti, T. Suntio, *IEEE Trans. Power Electron.* **2013**, *28*, 3028.
- [26] R. Khanna, Q. Zhang, W. E. Stanchina, G. F. Reed, Z. H. Mao, *IEEE Trans. Power Electron.* **2014**, *29*, 1490.
- [27] S. Bhattacharyya, *Sustainable Energy* **2021**, *12*, 293.
- [28] S. Manna, D. K. Singh, A. K. Akella, *Int. J. Adapt. Control Signal Process.* **2023**, *1*, <https://doi.org/10.1002/acs.3684>.
- [29] D. K. Singh, A. K. Akella, S. Manna, *Electr. Eng.* **2023**, <https://doi.org/10.1007/s00202-023-01922-3>.
- [30] M. Dehghani, M. Taghipour, G. B. Gharehpetian, M. Abedi, *J. Mod. Power Syst. Clean Energy* **2021**, *9*, 376.
- [31] D. K. Singh, S. Manna, A. K. Akella, *Lect. Notes Electr. Eng.* **2022**, *852*, 157.
- [32] G. V. Hollweg, P. J. D. de Oliveira Evald, E. Mattos, L. C. Borin, R. V. Tambara, H. A. Gründling, W. Su, *IEEE Trans. Ind. Electron.* **2023**, *71*, 2978.
- [33] K. R. Sorto-Ventura, M. Abarzadeh, K. Al-Haddad, L. A. Dessaint, *IEEE Open J. Ind. Electron. Soc.* **2020**, *1*, 127.